JOURNAL OF AIRCRAFT
Vol. 34, No. 3, May–June 1997

Response, Loads, and Stability of Interconnected Rotor–Body Systems

J. K. Suresh*
Hindustan Aeronautics, Ltd., Bangalore 560 017, India
and
J. Nagabhushanam†
Indian Institute of Science, Bangalore 560 012, India

A rotor–body system with blades interconnected through viscoelastic elements is analyzed for response, loads, and stability in propulsive trim in ground contact and under forward-flight conditions. A conceptual model of a multibladed rotor with rigid flap and lag motions, and the fuselage with rigid pitch and roll motions is considered. Although the interconnecting elements are placed in the in-plane direction, considerable coupling between the flap–lag motions of the blades can occur in certain ranges of interblade element stiffness. Interblade coupling can yield significant changes in the response, loads, and stability that are dependent on the interblade element and rotor–body parameters. Ground resonance stability investigations show that by tuning the interblade element stiffness, the ground resonance instability problem can be reduced or eliminated. The interblade elements with damping and stiffness provide an effective method to overcome the problems of ground and air resonance.

Nomenclature

a	= lift-curve slope, rad
C_D	= sectional drag coefficient
C_{IB}	= damping coefficient of interblade element
C_β	= flap blade root damping coefficient
C_ξ	= lag blade root damping coefficient
e	= blade hinge offset
F_{IB}	= interblade element force/$\rho_a \pi R_b^4 \Omega^2$
h	= offset from lag hinge to interblade element attachment point
I_b	= mass moment of inertia of blade at hinge
K_{IB}	= linear stiffness of interblade element
K_β, K_ξ	= stiffness of flap and lag root springs at hinge
M_{IB}	= mass of interblade element (m_{IB} per unit length)
M_ξ	= lag root moment/$I_b\Omega^2$
N_b	= number of blades
R_e	= flap–lag structural coupling parameter
$\boldsymbol{r}_{hi,i\pm 1}$	= vector for interblade element between ith and $(i \pm 1)$th blades
α_N	= interblade spacing, $2\pi/N_b$
α_p, α_r	= fuselage pitch and roll angles
β_{i-1}, β_i, β_{i+1}	= flap angle of $(i - 1)$th, ith, $(i + 1)$th blades
γ	= lock number
μ	= advance ratio
μ_{IB}	= interblade element mass parameter
ξ_{i-1}, ξ_i, ξ_{i+1}	= lag angle of $(i - 1)$th, ith, $(i + 1)$th blades
ψ_{i-1}, ψ_i, ψ_{i+1}	= azimuth angle of $(i - 1)$th, ith, $(i + 1)$th blades
Ω	= rotor speed, nominal
ω_h	= interblade element stiffness parameter
ω_p, ω_r	= body pitch and roll frequencies
$\omega_{\xi 0}$, $\omega_{\beta 0}$	= fundamental nondimensional lead–lag and flap natural frequencies in rotating coordinate system
$\bar{\ }$	= nondimensional quantity, ( )/R
$\dot{\ }$	= time derivative, $\partial(\ )/\partial t$ or $\partial(\ )/\partial\psi$

Introduction

VERY few rotor designs with interconnected rotor blades, which are essentially adopted to improve the ground resonance characteristics of the helicopter, are currently in existence. Recently, the French helicopter industry tested rotors with interconnected blades. Viscoelastic elements were used as interconnecting elements. It was observed that these rotor designs can lead to helicopters with good ground resonance characteristics, decreased flight loads, extended flight envelope, reduced weight and cross section, and lower vibrational levels.[1,2]

Although there are some helicopters in existence with interconnected blades, hardly any literature is available on their response, loads, and stability characteristics that is needed to fully understand, evaluate, and exploit the potential of their designs. The limited literature available[3–5] essentially illustrate the advantages of interblade dampers for improving ground resonance behavior with simple models. However, the successful implementation of interblade systems in an actual helicopter needs further studies of their effects on the response, loads, and stability characteristics of the helicopter.

Recently, the governing equations for a conceptual model of such a rotor having rigid blades with flap–lag motions and interconnected with viscoelastic elements were developed.[6] Although it is recognized that the rigid blade model is not sufficiently representative enough for the computation of the response and loads of the system, it can bring out some of the qualitative differences between the interconnected and noninterconnected configurations with the variation of interblade element parameters. Using these equations, an isolated rotor with interblade connections was investigated in hover and forward flight under moment trim conditions.[7] This investigation has brought out that interblade elements introduce nonlinear coupling between flap and lag motions of the blades, and that this coupling becomes significant in certain ranges of the interblade element and rotor parameters. Extensive results on the structural dynamics of the rotor, response, loads, and stability

Received April 29, 1996; revision received Dec. 27, 1996; accepted for publication Jan. 17, 1997.

*Manager, Helicopter Design Bureau.
†Professor, Department of Aerospace Engineering.

of the rotor in flight are presented with variation of interblade element and rotor parameters.

In the present study, an interconnected rotor–body system in ground contact and in air is investigated for the rotor response and loads, and stability of the various rotor–body modes under the variation of rotor, body, and interblade element parameters.

Analytical Model

The conceptual model of an N_b-bladed rotor with interconnected blades is presented in Fig. 1. The rotor blades are idealized as rigid with flap–lag motions executed about a coincident hinge located at a distance e from the hub center. The flap and lead–lag motions are restrained at the hinge by root springs of stiffness K_β and K_ξ, respectively, as defined in Ref. 8. A viscoelastic element with axial stiffness K_{IB}, mass per unit length m_{IB}, and viscous damping coefficient C_{IB} is connected between the blades. The ends of the interblade element are assumed to be hinged to the blades at a distance h from the coincident hinge location. No additional degrees of freedom are assigned to the viscoelastic elements. In addition, each rotor blade is assumed to be connected to the rotor hub through lag and flap rotational dampers (not shown in the figure) with viscous damping coefficients C_ξ and C_β, respectively. The rotor aerodynamic forces are obtained from linear, incompressible potential flow, thin airfoil theory with the wake-model flow treated explicitly through a finite state dynamic wake model.[9] For the present investigation, the dynamic wake model is restricted to consider three wake states. The fuselage is modeled as a symmetric rigid body with two degrees of freedom corresponding to the pitch and roll motions executed about the lateral and longitudinal axes of the fuselage. The c.m. of the rotor–body system is assumed to be longitudinally offset from the hub centerline by an amount X_{CG}. While idealizing the rotor–body system in ground contact, the contact stiffnesses between the landing gear and the ground are represented by rotational springs connecting the c.m. of the helicopter with the ground. No offset between the aerodynamic center and the c.m. of the fuselage is considered.

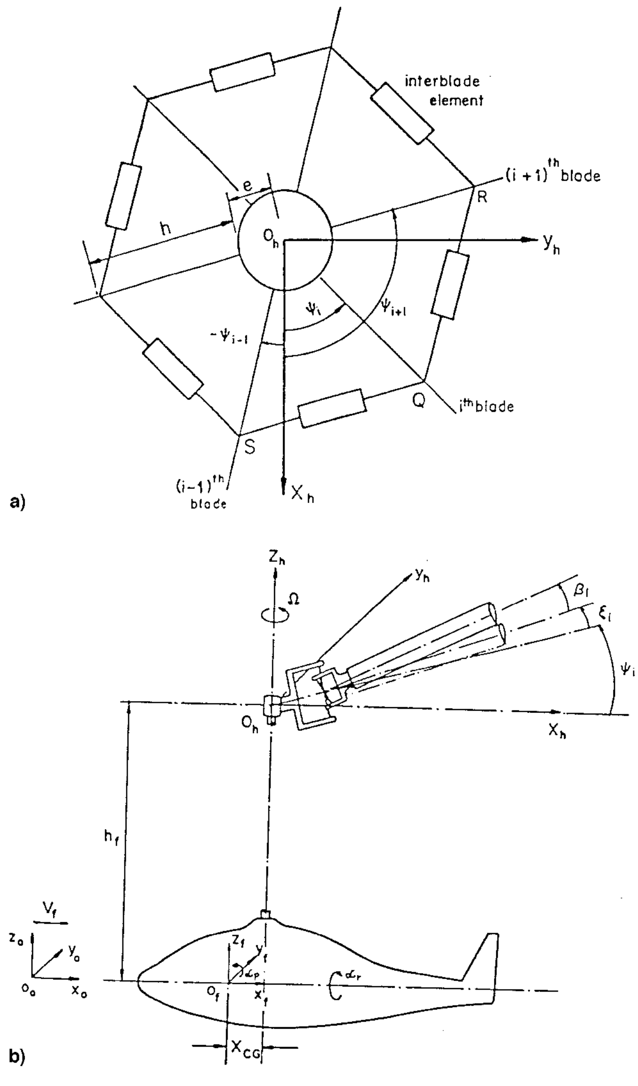

Fig. 1 Schematic of a) interconnected rotor blades with viscoelastic elements and b) the rotor–body system.

The basic governing differential equations of motion of the rotor blade are obtained using the Lagrangian approach. In the derivations, the governing variables and their time derivatives are assigned a uniform order of magnitude ε. The governing equations are formed by retaining terms up to and including order of magnitude ε^2. The resulting equations are extremely lengthy when expressed in their explicit form. Since the manual derivation of these equations is extremely difficult and prone to human errors, a special purpose symbolic processor, dynamic equations for helicopter interpretative models-version 2 (DEHIM-2) (Ref. 10) was used to derive the equations. In the derivation of the governing equations, the basic inputs for the symbolic processor are the transformation matrices corresponding to the motions of the system and the helicopter flight velocity with respect to the reference coordinate system. With user-described commands, the symbolic processor generates the expressions for potential and kinetic energies, Rayleigh dissipation functions, and virtual work of the system. Using these, the governing equations of motion are derived through the Lagrangian approach. The governing equations are nonlinearly coupled with periodic coefficients, and they are given next.

Rotor–Body Equations

The equations governing the flap, lag, pitch, and roll motions of the rotor–body system are presented in a compact symbolic form:

$$M_{\beta i} + (P - 1)\beta_i + Z\xi_i + C_\beta\dot{\beta}_i + M_{\beta,\mathrm{IN}} + M_{\beta,\mathrm{ST}} + M_{\beta,D} = M_{a,\beta i}$$

$$(i = 1, N_b)$$

$$M_{\xi i} + W\xi_i + Z\beta_i + C_\xi\dot{\xi}_i + M_{\xi,\mathrm{IN}} + M_{\xi,\mathrm{ST}} + M_{\xi,D} = M_{a,\xi i}$$

$$(i = 1, N_b)$$

$$M_{\alpha p} + M_{\alpha p,\mathrm{IN}} + M_{\alpha p,\mathrm{ST}} + M_{\alpha p,D} = M_{a,\alpha p}$$

$$M_{\alpha r} + M_{\alpha r,\mathrm{IN}} + M_{\alpha r,\mathrm{ST}} + M_{\alpha r,D} = M_{a,\alpha r}$$

Symbolically, $M_{\beta i}$, $M_{\xi i}$, $M_{\alpha p}$, and $M_{\alpha r}$ denote the inertial terms and $M_{a,\beta i}$, $M_{a,\xi i}$, $M_{a,\alpha p}$, and $M_{a,\alpha r}$ denote the aerodynamic terms in the respective equations. Further, $M_{\beta,\mathrm{IN}}$, $M_{\xi,\mathrm{IN}}$, $M_{\alpha p,\mathrm{IN}}$, $M_{\alpha r,\mathrm{IN}}$, $M_{\beta,\mathrm{ST}}$, $M_{\xi,\mathrm{ST}}$, $M_{\alpha p,\mathrm{ST}}$, $M_{\alpha r,\mathrm{ST}}$, and $M_{\beta,D}$, $M_{\xi,D}$, $M_{\alpha p,D}$, $M_{\alpha r,D}$ represent the expressions that describe the terms arising in the flap, lag, and body motions because of the introduction of interblade connecting elements. These expressions are very lengthy and have numerous terms. They introduce coupling between motions of the different blades and the body through the mass, stiffness, and damping parameters of the interblade element. A typical intermediate expression for $M_{qi,\mathrm{ST}}$ and $M_{qi,D}$ that represents the terms in the equations arising from the stiffness and damping of interblade connections is given next:

$$M_{qi,\mathrm{ST}} = \frac{K_{\mathrm{IB}}}{I_b\Omega^2}\left\{\left[\frac{\Delta L_p}{L_p}\right]\left[\boldsymbol{r}_{hi,i+1}\cdot\frac{\partial \boldsymbol{r}_{hi,i+1}}{\partial q_i}\right] + \left[\frac{\Delta L_m}{L_m}\right]\left[\boldsymbol{r}_{hi,i-1}\cdot\frac{\partial \boldsymbol{r}_{hi,i-1}}{\partial q_i}\right]\right\}$$

$$M_{qi,D} = \frac{C_{\mathrm{IB}}}{I_b\Omega^2}\left\{\frac{[\dot{\boldsymbol{r}}_{hi,i+1}\cdot\boldsymbol{r}_{hi,i+1}]}{L_p^2}\left[\boldsymbol{r}_{hi,i+1}\cdot\frac{\partial \boldsymbol{r}_{hi,i+1}}{\partial q_i}\right] + \frac{[\dot{\boldsymbol{r}}_{hi,i-1}\cdot\boldsymbol{r}_{hi,i-1}]}{L_m^2}\left[\boldsymbol{r}_{hi,i-1}\cdot\frac{\partial \boldsymbol{r}_{hi,i-1}}{\partial q_i}\right]\right\} \qquad (qi = \beta_i, \xi_i, \alpha_p, \alpha_r)$$

where $\boldsymbol{r}_{hi,i\pm1}$ is the vector joining the interblade element attachment points of the ith with $(i+1)$th and $(i-1)$th blades given by

$$\begin{aligned}
\boldsymbol{r}_{hi,i\pm1} = {} & h\{(1+(\bar{e}/\bar{h}))(1-0.5\alpha_p^2)(\cos(\psi_i)-\cos(\psi_{i\pm1})) \\
& -\alpha_p(\beta_i-\beta_{i\pm1}) - 0.5(\beta_i^2\cos(\psi_i)-\beta_{i\pm1}^2\cos(\psi_{i\pm1}) \\
& +\xi_i^2\cos(\psi_i)-\xi_{i\pm1}^2\cos(\psi_{i\pm1})) - (\xi_i\sin(\psi_i) \\
& -\xi_{i\pm1}\sin(\psi_{i\pm1}))\}\hat{i} + h\{(1+(\bar{e}/\bar{h}))[(1-0.5\alpha_r^2)(\sin(\psi_i) \\
& -\sin(\psi_{i\pm1})) - \alpha_r\alpha_p(\cos(\psi_i)-\cos(\psi_{i\pm1}))] + (\xi_i\cos(\psi_i) \\
& -\xi_{i\pm1}\cos(\psi_{i\pm1})) - 0.5(\xi_i^2\sin(\psi_i)-\xi_{i\pm1}^2\sin(\psi_{i\pm1}) \\
& +\beta_i^2\sin(\psi_i)-\beta_{i\pm1}^2\sin(\psi_{i\pm1})) - \alpha_r(\beta_i-\beta_{i\pm1})\}\hat{j} \\
& +h\{(1+(\bar{e}/\bar{h}))[\alpha_p(\cos(\psi_i)-\cos(\psi_{i\pm1})) \\
& +\alpha_r(\sin(\psi_i)-\sin(\psi_{i\pm1}))] - \alpha_p(\xi_i\sin(\psi_i)-\xi_{i\pm1}\sin(\psi_{i\pm1})) \\
& +\alpha_r(\xi_i\cos(\psi_i)-\xi_{i\pm1}\cos(\psi_{i\pm1})) + \beta_i - \beta_{i\pm1}\}\hat{k}
\end{aligned}$$

$L_0 = 2h\sin(\alpha_N/2)$ is the undeformed length of the interblade element, $L_p = |\boldsymbol{r}_{hi,i+1}|$, $L_m = |\boldsymbol{r}_{hi,i-1}|$, $\Delta L_p = L_p - L_0$, $\Delta L_m = L_m - L_0$. $\hat{i}$ $\hat{j}$, and $\hat{k}$ correspond to the unit vectors in the inertial coordinate system. These expressions are subsequently evaluated to the specified order of magnitude in the governing equations. The explicit description of the previous equations is available in Ref. (11).

Inflow Equations

In the inflow equations, the inflow over the disc $\lambda(\bar{r}, \psi, t)$ is represented by a complete set of functions comprising radial shape functions $\phi_j^s(\bar{r})$ [$=\bar{P}_j^s(\nu)/(\nu)$, where $\nu = \sqrt{(1-\bar{r}^2)}$, and $\bar{P}_j^s$ are the normalized Legendre functions], azimuthal harmonics $\cos(s\psi_i)$ and $\sin(s\psi_i)$ and the associated inflow states, viz., the cosine-component states $\alpha_j^s(t)$ and the sine-component states $\beta_j^s(t)$, which act like degrees of freedom. Now, the inflow can be expressed as

$$\lambda(\bar{r},\psi,t) = \sum_{s=0}^{\infty}\sum_{j=s+1,s+3}^{\infty}\phi_j^s(\bar{r})[\alpha_j^s(t)\cos(s\psi) + \beta_j^s(t)\sin(s\psi)]$$

The dynamic wake equations are given by

$$[M]\{\dot{\alpha}_j^s\} + [V_c][L_c]^{-1}\{\alpha_j^s\} = \tfrac{1}{2}\{\tau_n^{mc}\}$$

$$[M]\{\dot{\beta}_j^s\} + [V_s][L_s]^{-1}\{\beta_j^s\} = \tfrac{1}{2}\{\tau_n^{ms}\}$$

In these equations, the linear operator $[M]$ denotes the apparent mass matrix and is a pure diagonal matrix, and the operators $[L_c]$ and $[L_s]$ denote the cosine and sine influence coefficient matrices, respectively. Closed-form solutions are available for $[M]$, $[L_c]$, and $[L_s]$. On the right-hand sides of the equations, $[\tau_n^{mc}]$ and $[\tau_n^{ms}]$ represent cosine and sine components of the pressure coefficients or the inflow forcing functions, respectively. These functions are given for a rotor with N_b blades by

$$\tau_n^{0c} = \frac{1}{2\pi}\sum_{i=1}^{N_b}\int_0^1 \bar{L}_i\frac{\bar{P}_n^0(\nu)}{\nu}\,\mathrm{d}\bar{r}$$

$$\tau_n^{mc} = \frac{1}{\pi}\sum_{i=1}^{N_b}\int_0^1 \bar{L}_i\frac{\bar{P}_n^m(\nu)}{\nu}\cos(m\psi_i)\,\mathrm{d}\bar{r}$$

$$\tau_n^{ms} = \frac{1}{\pi}\sum_{i=1}^{N_b}\int_0^1 \bar{L}_i\frac{\bar{P}_n^m(\nu)}{\nu}\sin(m\psi_i)\,\mathrm{d}\bar{r}$$

where $\bar{L}_i = L_i/\rho_a\Omega^2R^3$ is the nondimensional blade sectional circulatory lift per unit span.

The diagonal matrices $[V_c]$ and $[V_s]$ correspond to the flow parameters. The (1,1) element of $[V_c]$ is given by $V_T = \sqrt{(\mu^2+\lambda_T^2)}$, and all other elements of $[v_c]$ and $[v_s]$ are given by $V = [\mu^2 + (\lambda_T + \lambda_m)\lambda]/\sqrt{(\mu^2+\lambda_T^2)}$. Here, λ_T represents the total inflow (freestream plus thrust-induced inflow) and λ_m represents thrust-induced inflow $C_T/(2V_T)$. For additional details see Ref. 12.

Results and Discussion

The nonlinear equations of motion of the rotor–body system are coupled with the equations of equilibrium of forces and moments of the rotor–body in flight and are solved under the propulsive trim condition. Using the equations, the rotor–body system trim and response parameters are iteratively computed using the autopilot trim method.[13] Stability investigations are carried out with perturbed linear equations about the periodic equilibrium state. The damping of the system is computed from the eigenvalues of the Floquet transition matrix. The modes are identified based on the dominant multiblade flap and lag motions, and the body motions.[14]

The interblade element stiffness and mass parameters are represented by nondimensional parameters ω_h $\{=K_{\mathrm{IB}}h^2/I_b\Omega^2\}^{1/2}$ and μ_{IB} $\{=M_{\mathrm{IB}}h^2/I_b\}$, respectively. The interblade damping parameter ζ_{IB} is represented in terms of percentage of the critical damping based on the nonrotating lag mode frequency. The baseline and range of variation of the parametric values used in the investigation are given in Table 1. It may be noted that the baseline corresponds to a noninterconnected rotor. Whenever a parametric value other than that corresponding to the baseline is used, its value is indicated in the figure.

The discussion on response and loads corresponds to the blade flap and lag root moments, interblade element force, and the lag moment distribution over the blade span with the variation of interblade stiffness under various flight conditions. The discussion on stability corresponds to multiblade lag and body mode damping with variation of interblade stiffness for conditions of rotor–body system in ground contact and in flight.

Flap Response

Flap response in terms of flap root moment with azimuth is shown in Fig. 2 for $N_b = 3$ for different ω_h. Introduction of the interblade element not only causes direct coupling between the lag motions of the blades, but also causes coupling with the flap motions of the blades. With rotor coning, the interblade element is compressed and the resulting force in the element is a function of ω_h and N_b for a given cone angle.[7] When the blade tries to flap, a component of the force in the interblade element tends to reduce the flapping motion, resulting in an apparent increase in flapping stiffness. As a consequence, compared to the baseline case $\omega_h = 0$, the flap response decreases in hover with an increase of ω_h. The trends of azimuthal flap response in forward flight with ω_h are very similar to those of the baseline, except for their decreased magnitude in most of the rotation.

Table 1 Description of baseline parameters

Parameter	Baseline	Range of variation
N_b	3	3–6
Rotor solidity σ	0.08	——
γ	7	——
$\bar{e}$	0.0	——
c.g. offset $\bar{X}_{c.g.}$	0.0	——
Offset between rotor head and fuselage c.g. $\bar{h}_f$	0.25	——
Fuselage inertias		
I_{xx}/I_b	6	——
I_{yy}/I_b	25	——
I_{xz}/I_b	5	——
Nondimensional natural frequencies		
Flap $\omega_{\beta O}$	1.05	——
Lag $\omega_{\xi O}$	0.35	0.1–0.9
Pitch (ground resonance) ω_p	0.7	0.15–0.65
Roll (ground resonance) ω_r	0.8	0.25–0.75
R_e	0.0	——
Blade loading C_T/σ	0.1	0.0125–0.1
a	2π/rad	——
Profile drag coefficient of blade section C_{dO}	0.01	——
Fuselage drag coefficient f	0.0125	——
μ	——	0–0.4
Equilibrium condition	Propulsive trim	——
Dynamic inflow model	3 × 3 model	——
Nondimensional interblade parameters		
Stiffness ω_h	0	0.0–2.0
Damping ζ_{IB}	0	0–4% critical
Mass μ_{IB}	0	——
Element attachment point from hinge h/R_b	0.1	——

Lag Response

The lag response in terms of lag root moments with azimuth for a three-bladed rotor is shown in Figs. 3a–3e for various ω_h under hover and forward-flight conditions. For $\mu = 0$ (Fig. 3a), collective mode response alone exists, and hence, the interblade stiffness does not influence the root moments. In forward flight (Figs. 3b–3e), for low ω_h, the lag moments are very close to that of the baseline. For $0.8 \leq \omega_h \leq 1.2$, the dynamic amplitudes of the moment significantly increase compared with case $\omega_h = 0.4$. Between the results of the response for $\omega_h = 0.8$ and $\omega_h = 1.2$, a phase shift of 180 deg is observed. The lag regressive mode frequency of the rotor, when viewed in the rotating coordinate system, has a value less than 1Ω for $\omega_h < 1$, and is greater than 1Ω for $\omega_h > 1$.[6,7] Since the dominant excitation force is of 1Ω, the response will change phase by 180 deg when $\omega_h > 1$. The high amplitude of the lag response observed in the region $0.8 \leq \omega_h \leq 1.2$ is because of the proximity of the lag mode frequency of the blade in the rotating system with that of the dominant excitation force. With a further increase of ω_h, although the dynamic amplitudes decrease and are close to the magnitude of the baseline case, we observe an increase of higher harmonic root moments.

Interblade Element Force

The variation of the interblade element force with azimuth for various ω_h is shown in Figs. 3f–3j for $N_b = 3$. In hover (Fig. 3f), although there is lag collective mode response, the interblade element shows a force that is constant over the azimuth. The interblade element force increases with ω_h. The interblade element force varies with azimuth in forward flight (Figs. 3g–3j), and its trend is dependent on ω_h. For low ω_h (=0.4), the dynamic amplitude of the interblade element force is quite small compared with that of $\omega_h = 0.8$. Compared to $\omega_h = 0.8$, a substantial increase of the dynamic amplitude of the interblade element force is observed with a phase shift of 180 deg for $\omega_h = 1.2$. In the region $0.8 \leq \omega_h \leq 1.2$, the increase in the dynamic amplitude of the interblade element force is because of the increased lag response. With a further increase of ω_h, higher harmonic force components become significant. The damping of the interblade element does not result in appreciable changes in the interblade element forces.

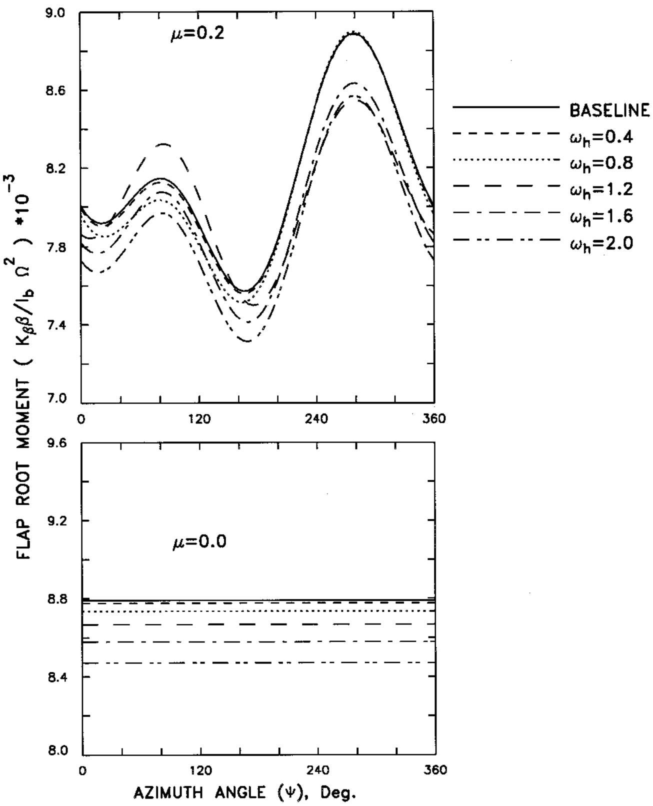

Fig. 2 Flap root moment with azimuth ($\omega_{\xi O} = 0.35$; $N_b = 3$).

Lag Moment Distribution over Blade Span

The lag moment distribution over the blade in hover for any ω_h will be the same as the baseline case because of the cancellation of the forces of interblade elements that are on either

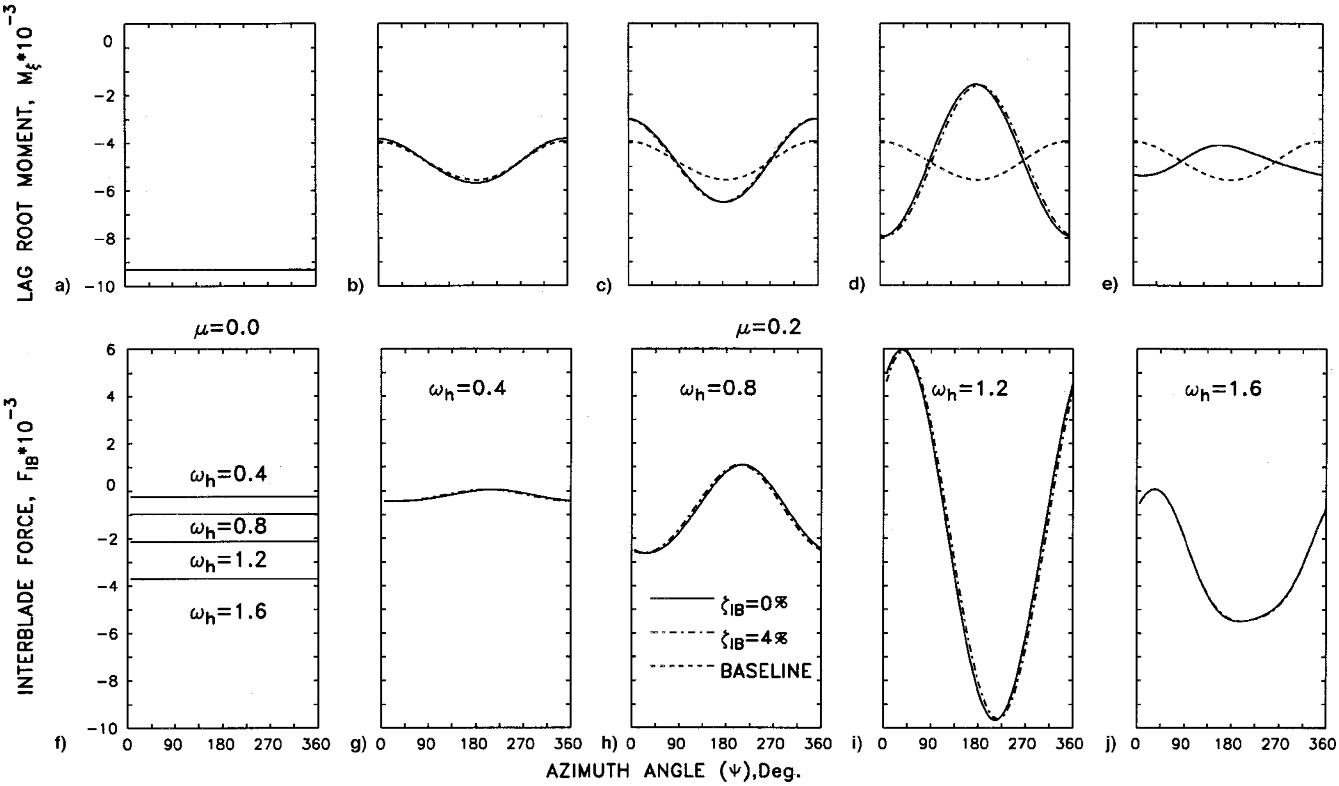

Fig. 3 Lag root moment and interblade element force with azimuth ($\omega_{\xi 0}$ = 0.35; N_b = 3).

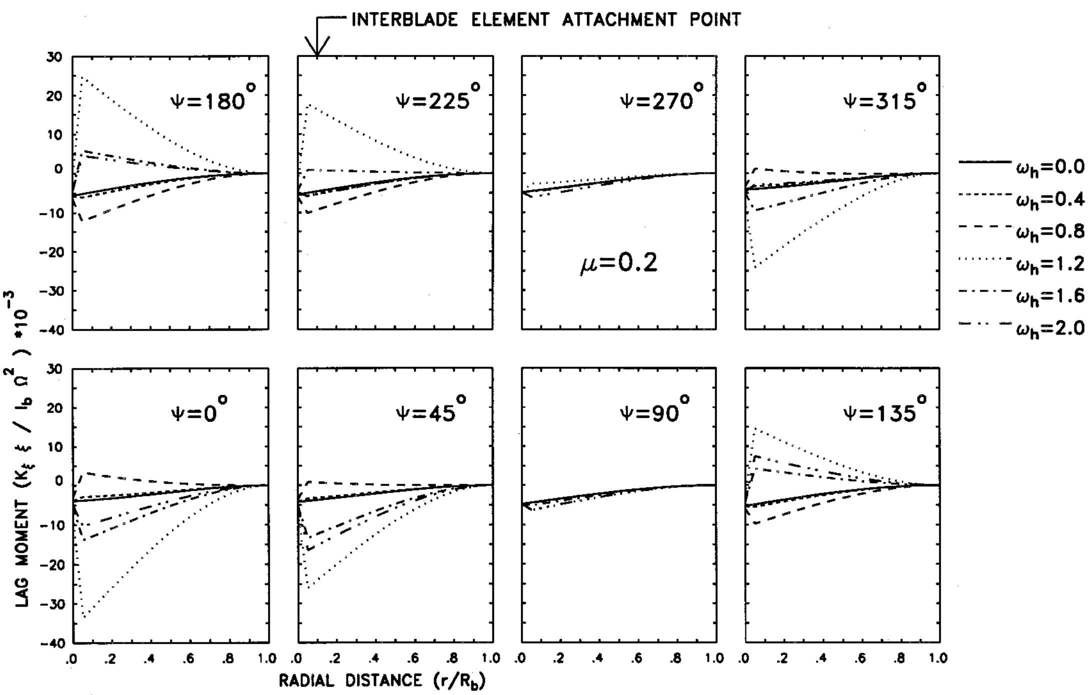

Fig. 4 Blade lag moment with radial distance ($\omega_{\xi 0}$ = 0.35; N_b = 3).

side of the blade. The variation of lag moment over the blade span is shown at different azimuthal locations for μ = 0.2 in Fig. 4 for N_b = 3. It is observed that the lag moment variation over the blade span shows a significant influence because of ω_h at all azimuths. The lag moment increases gradually from the tip, reaching a peak near the element attachment point, and drops steeply beyond this point. The cases where large moments are observed near the attachment point for certain azimuth stations correspond to the cases of high interblade element forces ($0.8 \leq \omega_h \leq 1.2$, see Fig. 3). Compared to the lag moment at the root, the moment near the attachment point for certain azimuth stations can be several times higher.

Stability

Aeromechanical stability analysis constitutes the most important investigation of the rotor–body system. It is characterized by the intense coupling between the rotor and body modes leading to the phenomena of ground and air resonance. The stability characteristics are governed by the blade flap and lag frequencies, body pitch and roll frequencies, location of the c.g. of the body with respect to rotor hub center, flight conditions, etc. Here, the stability characteristics of the rotor–body system are presented with a variation of the interblade element and the rotor–body system parameters.

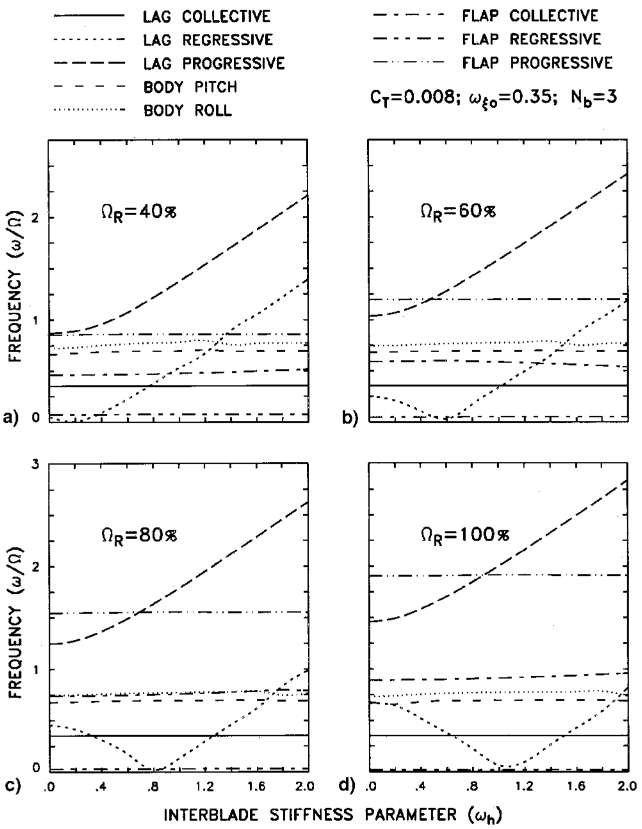

Fig. 5 Lag, flap, and body frequencies with interblade stiffness (ω_p = 0.7; ω_r = 0.8) (rotor–body system in ground contact).

Ground Resonance

The results of stability for the rotor–body system in ground contact are presented in Figs. 5–9.

Rotor Speed

Figure 5 represents the normalized frequencies of the flap and lag collective, regressive and progressive modes of the blades, and the body pitch and roll modes with the variation of ω_h at different rotor speeds. Figures 6 and 7 show the damping of the corresponding lag and body modes. For this study, the rotor–body system parameters considered are $\omega_{\xi 0} = 0.35$, $N_b = 3$, $\omega_p = 0.7$, $\omega_r = 0.8$, and $C_t = 0.008$. As expected, the collective mode damping increases with rotor speed and is least influenced by the variation of ω_h. The lag regressive mode damping (Fig. 7a), which is the crucial modal damping of the system, is found to be stable at all rotor speeds for all ω_h, except for the case of $\Omega_R = 100\%$. For this case, the lag regressive mode, which is highly unstable at $\omega_h = 0$, shows a steep recovery to a stable mode as ω_h is increased to about 0.38. For $\omega_h > 0.38$, the mode remains completely stable. From Fig. 5, we correspondingly observe that the lag regressive mode can have intense coupling with the body pitch mode in the region $0 < \omega_h < 0.3$. Beyond $\omega_h = 0.38$, another important feature observed for this mode, at all rotor speeds (Fig. 7a), is the steep decrease of damping up to a certain magnitude of ω_h followed by an increase with further increase of ω_h. This feature is also observed for the isolated rotor case,[7] and the reason for this phenomenon can be traced to the coupling of the lag regressive mode with the flap regressive mode (see Fig. 5). The lag progressive mode damping trends observed are similar to those of the isolated rotor[7] and the dip in the damping can be traced to the coupling of the lag progressive mode with the flap progressive mode (see Fig. 5).

The body pitch mode damping (Fig. 7b) is stable for all rotor speed cases throughout the range of ω_h. However, the 100% rotor speed case needs special mention. At $\omega_h = 0$, the pitch mode is extremely stable in contrast to the high instability exhibited by the lag regressive mode. In the region $0 < \omega_h <$

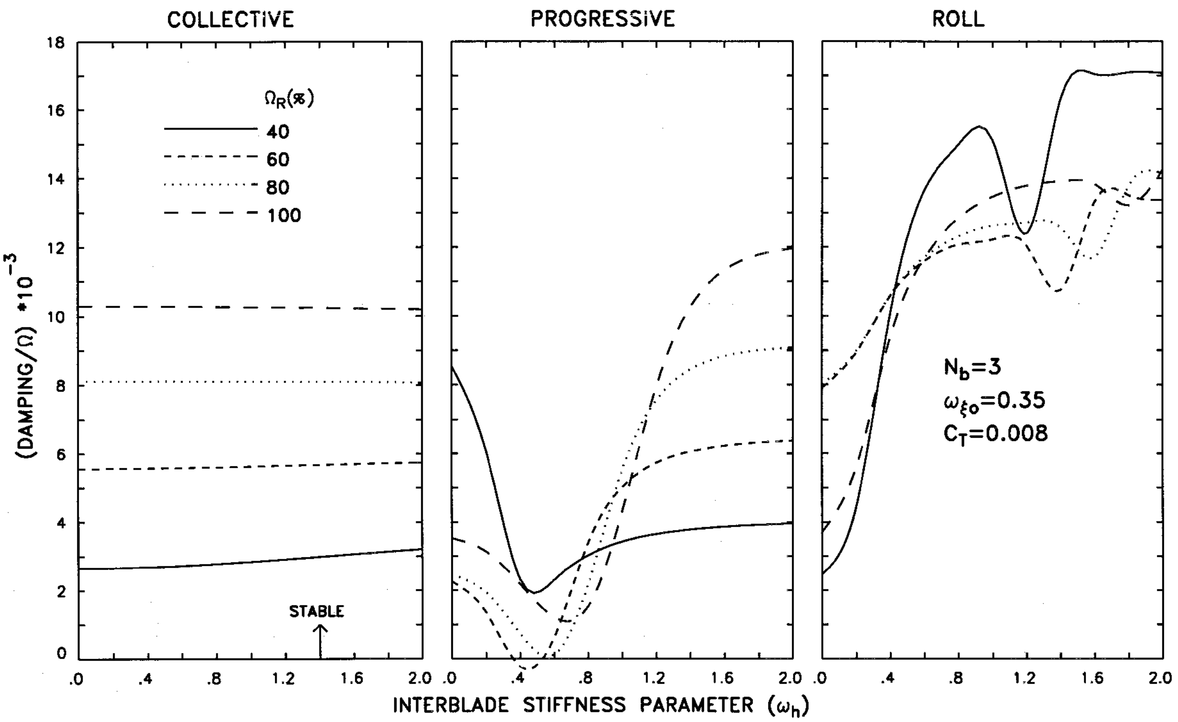

Fig. 6 Lag collective, progressive, and body roll mode dampings at various rotor speeds (ω_p = 0.7; ω_r = 0.8) (rotor–body system in ground contact).

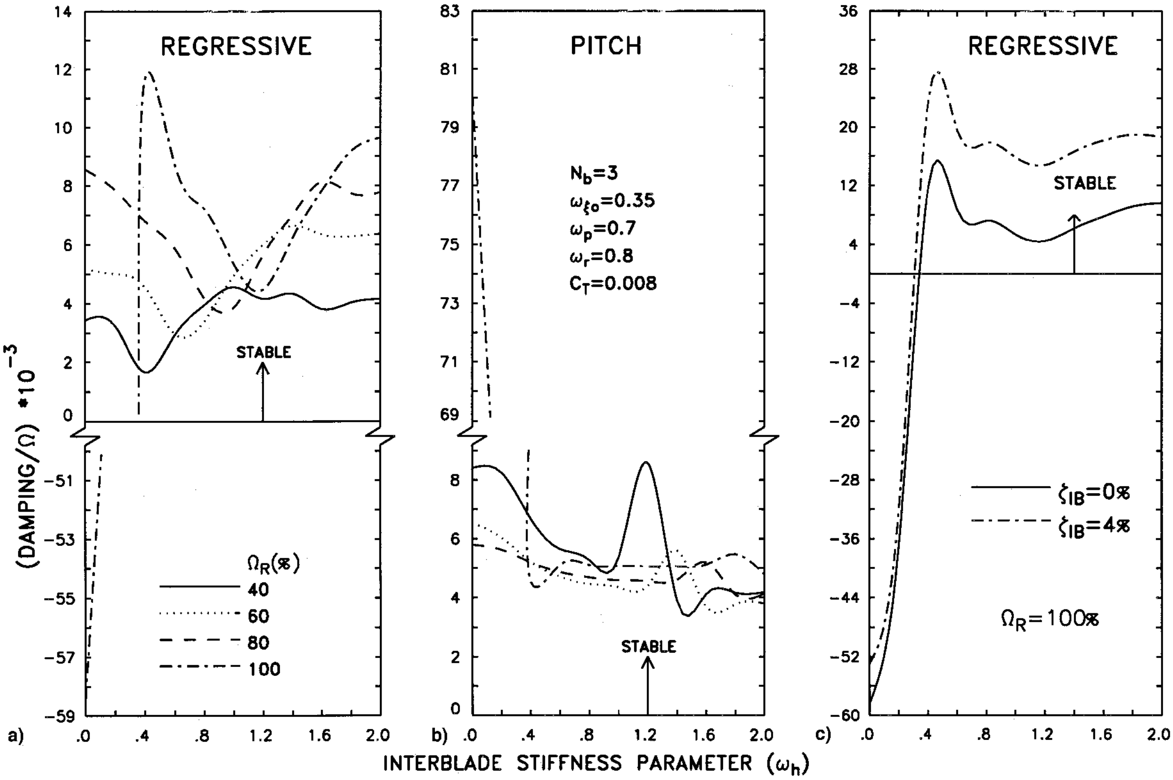

Fig. 7 Lag regressive and body pitch mode dampings with rotor speed (rotor–body system in ground contact).

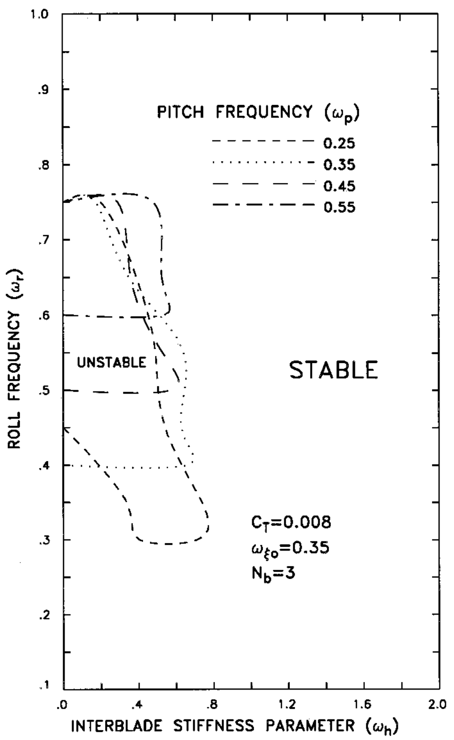

Fig. 8 Stability boundaries for lag regressive mode with body pitch frequency (rotor–body system in ground contact).

0.38, the pitch mode damping shows a steep decrease while still remaining stable, whereas the lag regressive mode damping increases steeply and finally becomes stable around ω_h = 0.38, as discussed earlier. The pitch mode once again shows an increase and decrease in damping in the region of ω_h = 1.8 because of its increased coupling with the lag regressive mode (see Fig. 5). For cases of rotor speed Ω_R < 100%, the increasing and decreasing trends of pitch mode damping with ω_h can be easily inferred from Fig. 5.

The body roll mode damping in general increases steeply in the region 0 < ω_h < 0.8. With a further increase of ω_h, the damping decreases and increases in certain regions of ω_h, which are dependent on the rotor speed case. These trends of damping can be traced to the increased coupling between the body roll mode and the lag regressive mode (see Fig. 5).

Figure 7c presents the lag regressive mode damping with ω_h and ζ_{IB} = 4% at 100% rotor speed. With the introduction of interblade damping, the lag regressive mode damping increases, which leads to the shifting of the damping trends bodily upward and toward the left of the trends of damping for case ζ_{IB} = 0%. This results in the mode becoming stable at a lower ω_h than for case ζ_{IB} = 0%, as well as in the increased damping of the system in the region of ω_h > 0.38.

In the following text the results are presented for the Ω_R = 100% case.

Stability Boundaries for Parameters $\omega_{\xi 0}$ and ω_h

As discussed earlier, the problem of ground resonance instability in a helicopter can be overcome by the introduction of interblade element stiffness. The ω_h required for this purpose is essentially dependent on the lag, pitch, and roll frequencies ($\omega_{\xi 0}$, ω_p, and ω_r). It is of interest to obtain the usable range of ω_h for which the rotor–body system is free from ground resonance instabilities for a given set of parametric values of $\omega_{\xi 0}$, ω_p, and ω_r. For this purpose, a set of stability boundary diagrams are generated wherein ω_h constitutes the abscissa and one of the parameters ω_r and $\omega_{\xi 0}$ constitute the ordinate. Figure 8 shows the stability boundaries for parameters ω_r and ω_h. In this study the rotating blade lag frequency is fixed at $\omega_{\xi 0}$ = 0.35, whereas different plots are generated for each assumed pitch frequency. It may be observed from the figure that beyond a certain value of ω_h (which depends on ω_r), the lag regressive mode is completely stable for all ω_h. For N_b = 3, Figs. 9a–9f show the stability boundaries with $\omega_{\xi 0}$ and ω_h. For Figs. 9a–9c, ω_p is varied with ω_r = 0.75, whereas for Figs. 9d–9f ω_r is varied with ω_p = 0.25. It may be noted that the various regions of instability seen in these figures essentially arise from the coupling between the lag regressive and the body pitch or roll modes. The coupling is also dependent on the number of blades in the rotor. The stability boundaries for $N_b = 3$, 4, and 5 presented in Fig. 9g for $\omega_r = 0.75$, $\omega_p = 0.45$ show that there can be significant differences in the regions of instability because of the interblade spacing. These figures provide information to tune the frequencies of the system for an interconnected rotor–body system to avoid ground resonance instabilities.

Air Resonance

The results of the investigations on air resonance stability of the rotor–body system with interconnected rotor blades in hover and forward flight are presented in Figs. 10–13.

Number of Blades and Interblade Element Damping

The damping of the lag and body modes are presented together with their frequencies in Fig. 10 for $\omega_{\xi 0} = 0.35$ for the hover case. It is observed that the lag regressive mode damping shows two dips in its variation with ω_h. From Fig. 10a, these dips can be attributed to the increased coupling of the lag regressive mode with the body roll motions. The lag progressive mode also shows a dip in its damping variation with ω_h, which can be attributed to the increased coupling of the mode with the flap progressive mode. The collective mode damping does not vary with ω_h as expected. The body mode consists of body roll and pitch motions coupled with flap motions of the blades. The damping is fairly constant over ω_h, except in the region around $\omega_h = 1.1$, where a mild dip in damping is observed. This dip in damping is caused by the mode getting further coupled with the lag regressive mode (see Fig. 10a). Figure 11 shows the results of the analysis in forward flight. The trends of damping variation of all the modes are similar to those of hover. However, they are modulated by the forward-flight aerodynamics, as seen, for example, at $\mu = 0.4$, where even the collective mode damping is significantly influenced by ω_h.

The variation of lag mode damping with ω_h for $N_b = 3$ and 4 is shown in Fig. 12 for $\mu = 0.2$, $\zeta_{IB} = 0$ and 4%. For $N_b = 3$ and 4, the trends of the lag collective, regressive, and progressive mode damping are similar to each other except for the different locations of the dips in damping, which arises from the parameter of interblade spacing.[7] With the introduction of interblade element damping, for both $N_b = 3$ and 4, the damping of these modes bodily move up, thus increasing their

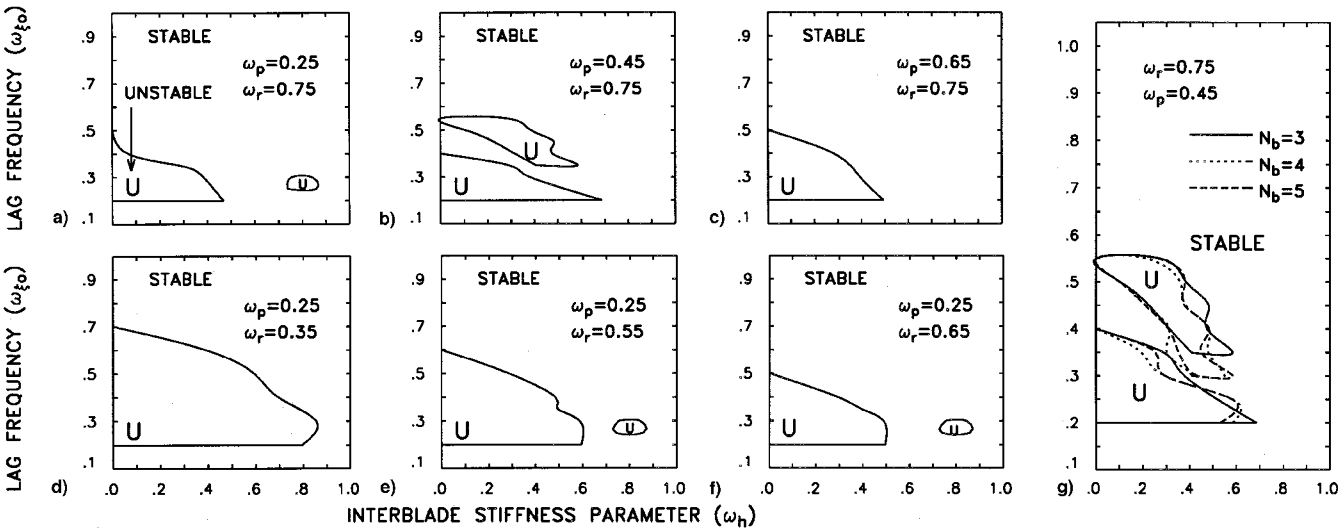

Fig. 9 Stability boundaries for lag regressive mode with lag mode frequency (C_T= 0.001) (rotor–body system in ground contact).

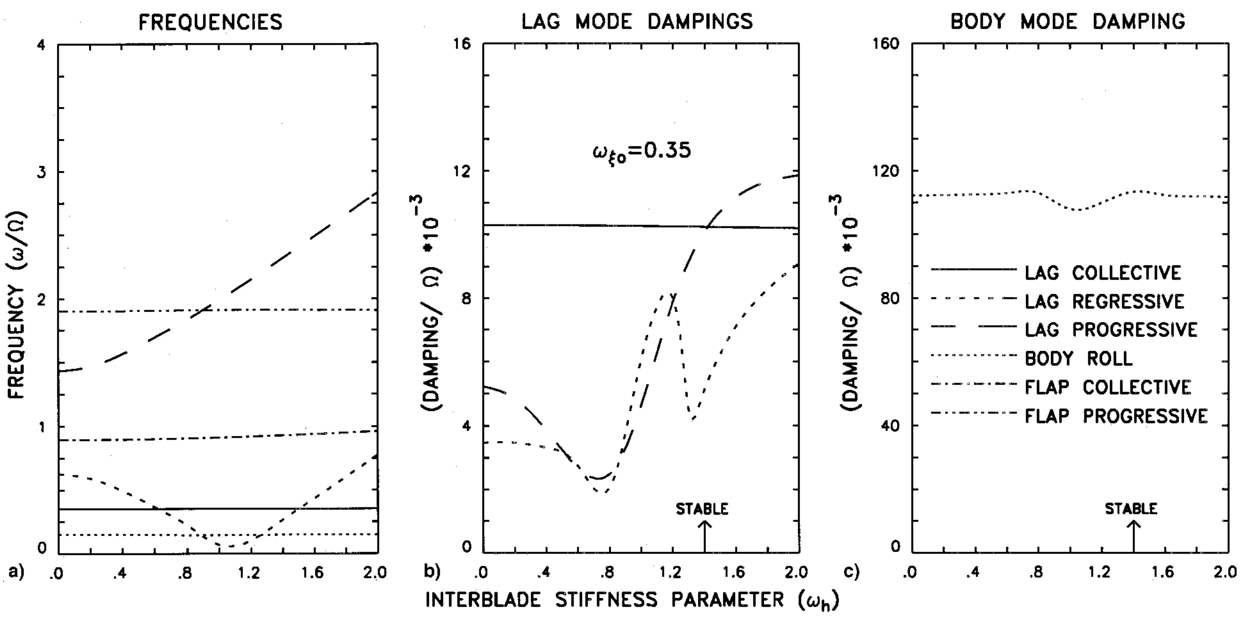

Fig. 10 Lag, flap, and body frequencies and dampings in hover (N_b = 3).

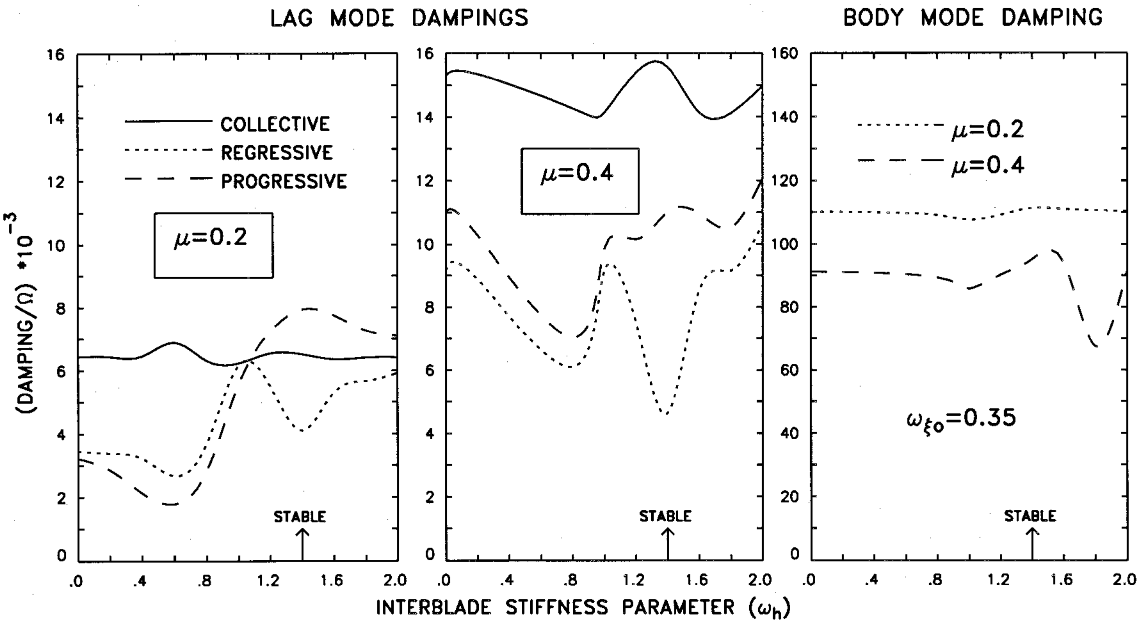

Fig. 11 Lag and body mode dampings in forward flight ($N_b = 3$).

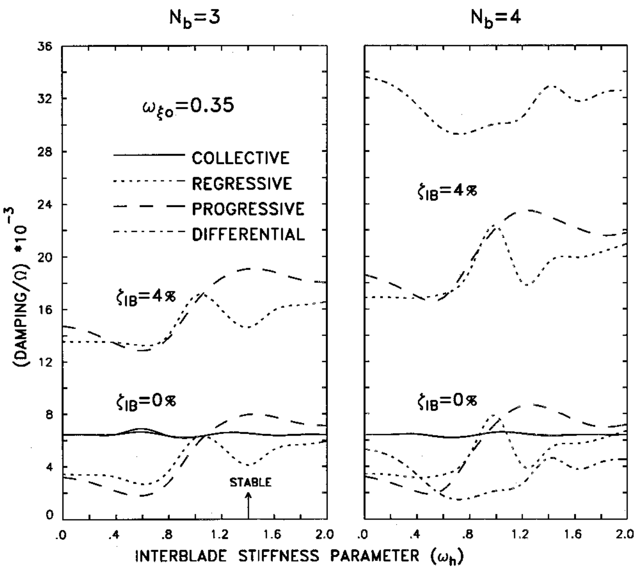

Fig. 12 Lag mode dampings with interblade element damping (μ = 0.2).

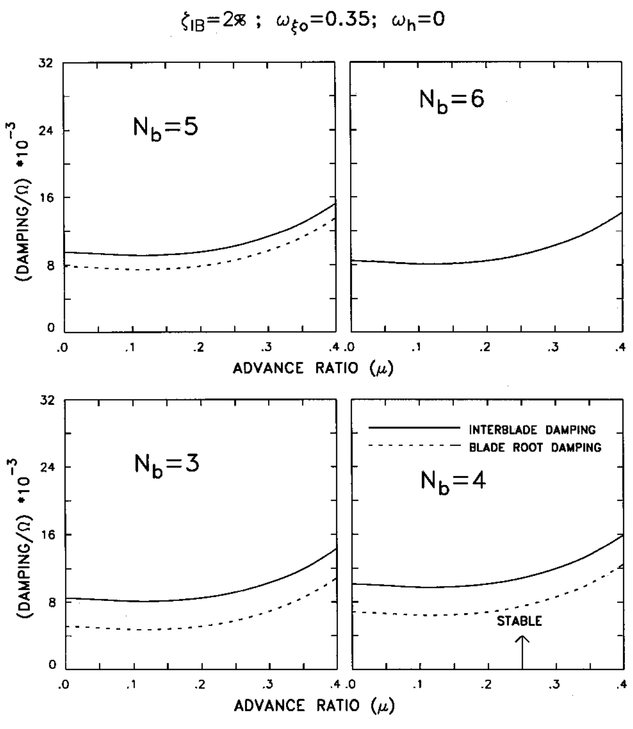

Fig. 13 Lag regressive mode dampings with blade root damping.

damping levels. The lag differential collective mode, typical of even-bladed rotors, shows lower damping compared to other modes in certain regions of ω_h for ζ_{IB} = 0%. However, the damping of this mode attains a higher level compared to the other modes with ζ_{IB} = 4%. This is because of the higher effectiveness of the interblade element damping for the lag differential mode as compared to the other modes. This can also be easily established by considering a simple linear rotor model with lag motions alone.[11]

Effectiveness of Interblade Dampers

A study is made to compare the lag mode damping of the system with N_b varied from 3 to 6 for two rotor–body idealizations, one with interconnected dampers (no interblade element stiffness), and the other with conventional dampers introduced at the blade root between the rotor blade and the hub, for various flight conditions. It may be noted that the damping moment for both the idealizations per unit lag angular velocity is kept the same. This leads to the equivalent hub damper parameter of magnitude $\zeta_{IB}\cos^2(\alpha_N/2)$, and it should be noted that the spanwise location of the interblade damper attachment to the rotor blade is the same for all the rotors. The results corresponding to the lag regressive mode damping for this study are presented in Fig. 13.

For case N_b = 3, because of the increased effectiveness of the lag damper connected between the blades, the lag regressive mode damping is substantially higher than the case of the blade-to-hub-connected damper. The increase in damping predicted for the interconnected damper system is close to those computed using Ref. 4. As N_b increases from 3 to 6, the effectiveness of the interconnected rotor for lag regressive mode damping decreases. For N_b = 6, the interconnected and non-interconnected rotors have the same lag regressive mode damping for the chosen geometry of the interconnected system.

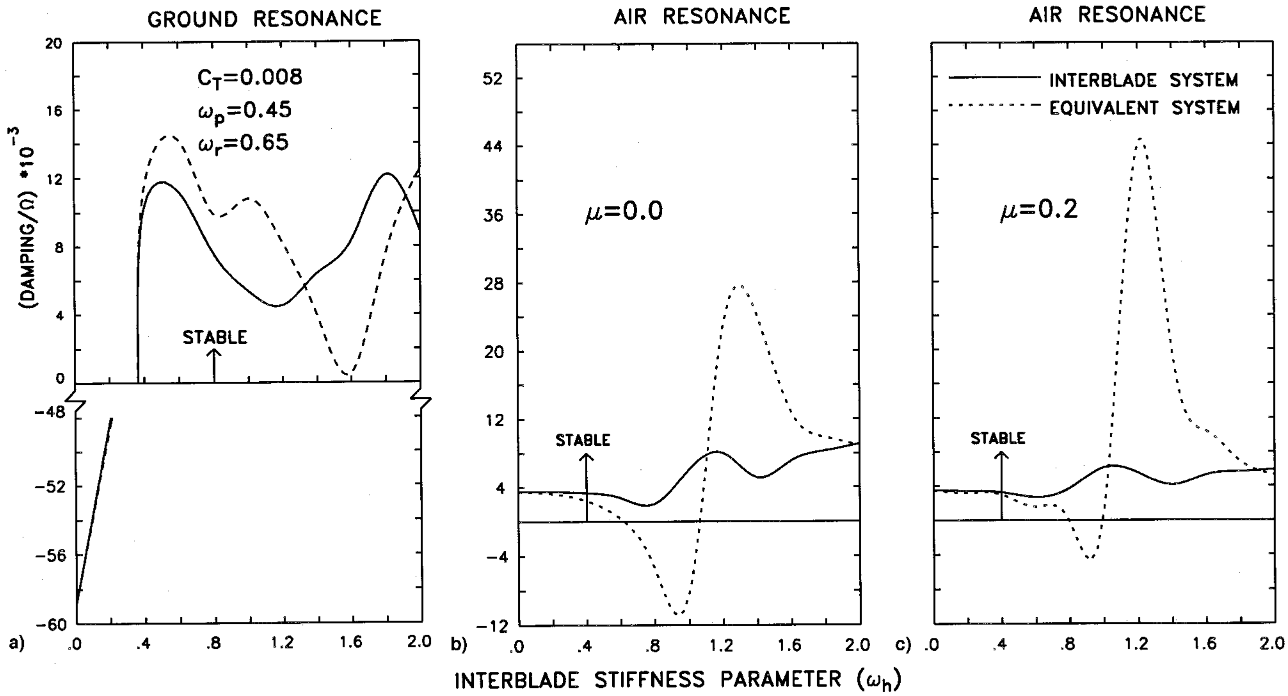

Fig. 14 Lag regressive mode damping with equivalent system representation ($\omega_{\xi 0}$ = 0.35; N_b = 3).

Equivalent System Representation

A study is made to assess whether the interconnected rotor blade system can be represented by an equivalent noninterconnected rotor system to obtain the crucial lag regressing mode damping using existing computational tools developed for noninterconnected rotor systems. Since the lag regressive mode frequency is a prime parameter of the stability of the system, the equivalent system can be represented by adjusting the rotating lag mode frequency of the blade to give a lag regressive (and also progressive) frequency equal to that of the interconnected rotor system.

Figure 14a gives a comparison of the lag regressive mode damping of an interconnected system with that of the corresponding equivalent system for the ground resonance. For small ω_h, the trends of damping predicted by the equivalent system representation is close to that of the interconnected system. However, the damping levels predicted by the equivalent system can be substantially in error for $\omega_h > 0.4$.

The damping variation of the lag regressive mode for the interconnected rotor is compared with that of the equivalent system in Figs. 14b and 14c in hover and forward flight for the air resonance. It is observed from the figure that both qualitatively and quantitatively, the damping computed from the equivalent system show gross variance from that of the interconnected rotor representation, more so at high ω_h and high forward speeds.

Basically, the interconnected and noninterconnected rotor systems are two different dynamic systems. However, for low ω_h, the damping corresponding to the two idealizations are close to each other, perhaps because of the feeble coupling between the lag motions of the blade.

Conclusions

The influence of interblade connecting elements on a rotor–body system in propulsive trim is studied for its response, loads, and stability in ground contact and in forward flight. The interblade elements, though placed in the plane of rotation, can yield significant coupling between the flap and lag motions of the blade in certain ranges of interblade element stiffness. Flap response (flap root moment) decreases with an increase of ω_h in all flight conditions. This decrease can be traced to an apparent increase of stiffness for flap motion because of the forces in the interblade elements. Lag root moments and interblade element forces can be significantly higher than the baseline in certain ranges of ω_h. For certain ranges of ω_h, the lag moment at the interblade attachment point can be several times higher than the root lag moment.

When the noninterconnected rotor–body system is unstable, it can be made stable by the introduction of interblade element stiffness. The amount of interblade stiffness needed to be introduced into the system depends on the number of blades in the rotor, blade flap and lag frequencies, and the body frequencies. Significant coupling is also observed between the flap and lag regressive modes in certain regions of ω_h, leading to trends of decrease and increase of lag regressive mode damping in these regions.

Air resonance studies show significant couplings between blade lag, flap and body motions leading to dips in the trends of lag regressive mode damping in certain regions of ω_h.

Interblade dampers are more effective than hub mounted dampers for $N_b \leq 6$ at all flight conditions. The equivalent representation with noninterconnected rotor–body system is valid for evaluating the lag regressive mode damping for low ω_h only.

References

[1]Guimbal, B., "Design, Evaluation and Proof of Concept Flights of a Main Rotor Interblade Viscoelastic Damping System," *Proceedings of the 14th European Rotorcraft Forum* (Milan, Italy), 1988, pp. 45-1–45-14.

[2]Serr, C., and Trouve, M., "Studying Dynamic Behaviour of X380 Helicopter Equipped with a New 5-Blade Composite Rotor," *Proceedings of the 47th Annual AHS National Forum* (Phoenix, AZ), American Helicopter Society, Alexandria, VA, 1991, pp. 997–1007.

[3]Mil', M. L., Nekrosov, A. V., Grodko, L. N., and Leykand, M. A., "Helicopters—Calculation and Design, Vol. II: Vibrations and Dynamic Stability," NASA TT F-519, Washington, DC, 1968, pp. 361–363.

[4]Sela, N. M., and Rosen, A., "Ground Resonance of a Helicopter with Inter-Connected Blades," *Journal of the American Helicopter Society*, Vol. 36, No. 2, 1991, pp. 82–85.

[5]Sela, N. M., and Rosen, A., "The Influence of Alternate Inter-Blade Connections on Ground Resonance," *Journal of the American Helicopter Society*, Vol. 39, No. 3, 1994, pp. 75–78.

[6]Suresh, J. K., Nagabhushanam, J., and Sampath, P., " Nonlinear

Governing Equations of Motion of Helicopter Rotor Blades with Interconnecting Viscoelastic Elements,'' *Journal of the Aeronautical Society of India*, Vol. 47, No. 1, 1995, pp. 13–24.

[7]Suresh, J. K., and Nagabhushanam, J., ''Response, Loads and Stability of Rotors with Interconnected Blades,'' *Journal of the American Helicopter Society*, Vol. 41, No. 4, 1996, pp. 283–290.

[8]Peters, D. A., '' Flap-Lag Stability of Helicopter Rotor Blades in Forward Flight,'' *Journal of the American Helicopter Society*, Vol. 20, No. 4, 1975, pp. 1–13.

[9]Peters, D. A., and He, C., ''A Closed Form Unsteady Aerodynamic Theory for Lifting Rotor in Hover and Forward Flight,'' *Proceedings of the 43rd Annual AHS National Forum* (St. Louis, MO), American Helicopter Society, Alexandria, VA, 1987, pp. 839–865.

[10]Manjunath, A. R., ''Rotor Stability in Hover and Forward Flight with a Generalized Dynamic Wake,'' Ph.D. Dissertation, Indian Inst. of Science, Bangalore, India, 1993.

[11]Suresh, J. K., ''Response, Loads and Stability of Helicopters with Interconnected Rotor Blades,'' Ph.D. Dissertation, Indian Inst. of Science, Bangalore, India, 1996.

[12]Peters, D. A., Boyd, D.B., and He, C. J.,''Finite State Induced Flow Mode for Rotors in Hover and Forward Flight,'' *Journal of the American Helicopter Society*, Vol. 34, No. 4, 1989, pp. 5–17.

[13]Peters, D. A., Kim, B. S., and Chen, H. S., ''Calculation of Trim Settings for a Helicopter Rotor by an Optimized Controller,'' *Journal of Guidance, Control, and Dynamics*, Vol. 7, No. 1, 1984, pp. 85–91.

[14]Nagabhushanam, J., and Gaonkar, G. H., ''Automatic Identification of Modal Damping Computed from Floquet Analysis,'' *Journal of the American Helicopter Society*, Vol. 40, No. 2, 1995, pp. 39–42.